

Measurement of the Casimir torque

David A. T. Somers^{1,2}, Joseph L. Garrett^{1,2}, Kevin J. Palm^{1,2} & Jeremy N. Munday^{1,2,3*}

Intermolecular forces are pervasive in nature and give rise to various phenomena including surface wetting¹, adhesive forces in biology^{2,3}, and the Casimir effect⁴, which causes two charge-neutral, metal objects in vacuum to attract each other. These interactions are the result of quantum fluctuations of electromagnetic waves and the boundary conditions imposed by the interacting materials. When the materials are optically anisotropic, different polarizations of light experience different refractive indices and a torque is expected to occur that causes the materials to rotate to a position of minimum energy^{5,6}. Although predicted more than four decades ago, the small magnitude of the Casimir torque has so far prevented direct measurements of it. Here we experimentally measure the Casimir torque between two optically anisotropic materials—a solid birefringent crystal (calcite, lithium niobite, rutile or yttrium vanadate) and a liquid crystal (5CB). We control the sign and strength of the torque, and its dependence on the rotation angle and the separation distance between the materials, through the choice of materials. The values that we measure agree with calculations, verifying the long-standing prediction that a mechanical torque

induced by quantum fluctuations can exist between two separated objects. These results open the door to using the Casimir torque as a micro- or nanoscale actuation mechanism, which would be relevant for a range of technologies, including microelectromechanical systems and liquid crystals.

Spatially separated, uncharged objects experience electromagnetic forces and torques due to quantum and thermal charge fluctuations. At small separations these phenomena are often called van der Waals effects and result from fluctuation-induced dipole-dipole interactions². At larger separations, greater than a few nanometres, the finite speed of light leads to retardation effects and an accompanying change in the distance dependence of the interaction, referred to as the Casimir (or Casimir–Lifshitz) regime^{4,7}. The van der Waals and Casimir effects both result from the same mechanism (quantum and thermal fluctuations), although historically they were derived from different physical pictures. A quantum-fluctuation-induced torque was predicted⁵ by considering materials with dielectric anisotropy (such as birefringent crystals); this short-range approximation was subsequently generalized⁶ to large separations. In addition to predictions of a torque arising

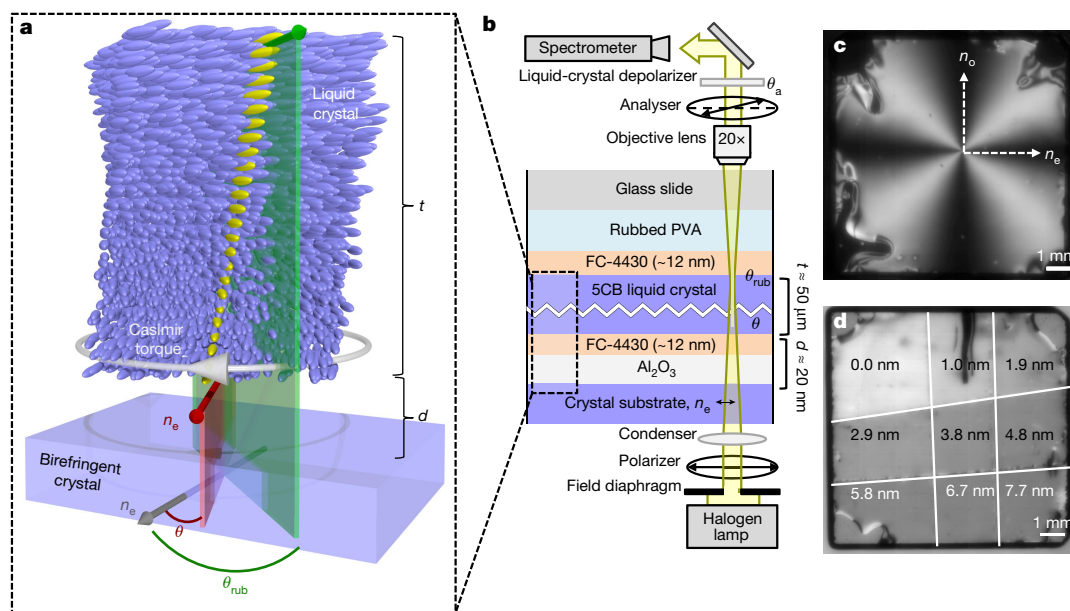


Fig. 1 | Apparatus measuring the Casimir torque. **a**, A birefringent crystal (with ordinary axis n_o and extraordinary axis n_e) causes a liquid crystal separated by a distance d to twist from θ_{rub} (anchoring at the top) to θ (final rotation angle) over a thickness $t \gg d$ (shown not to scale for clarity), owing to the Casimir torque. Yellow markers highlight the twist throughout the bulk of the liquid crystal. **b**, Schematic of the experimental set-up used to measure the torque (shown not to scale for clarity). Polarized white light from a halogen lamp is transmitted through the sample (with in-plane optical axes n_o and n_e parallel to the crystal surface) and detected via polarizing optics (containing a rotatable analyser at angle θ_a) and a spectrometer. The dashed box highlights the interacting surfaces

(liquid and solid birefringent materials separated by isotropic layers of Al_2O_3 and FC-4430). **c**, Optical micrograph of a cell with circularly rubbed PVA between crossed polarizers used to measure the dependence of the torque on θ (the angle between the principal axes of the two birefringent materials). A preferred twist of the liquid crystal towards the extraordinary axis of the substrate breaks the symmetry of the image, causing a compression of the horizontal dark regions and an expansion of the vertical dark regions. **d**, Image of a sample with linearly rubbed PVA with $\theta_{\text{rub}} = \theta_a = 45^\circ$ used to measure the dependence of the maximum torque on d at discrete, controlled separations. Lighter regions correspond to thinner Al_2O_3 layers (see labels for layer thickness) and stronger torques.

¹Department of Physics, University of Maryland, College Park, MD, USA. ²Institute for Research in Electronics and Applied Physics, University of Maryland, College Park, MD, USA. ³Department of Electrical and Computer Engineering, University of Maryland, College Park, MD, USA. *e-mail: jnmunday@umd.edu

from optical anisotropy of planar objects, a torque is also predicted to exist between objects with geometric anisotropy^{8,9}. Although the Casimir force has been the subject of many theoretical and experimental investigations^{10–19}, the torque has not yet been verified experimentally. Here we report measurements of the Casimir torque between anisotropic materials separated by tens of nanometres.

The Casimir torque depends on the dielectric function of the materials, which is generally evaluated at complex frequencies $\varepsilon(i\xi)$ (ref. 6). This torque causes the two objects to align their optical axes of higher refractive index and decays as roughly d^{-2} , where d is the distance between the materials. Several experimental designs have been proposed to measure the torque, including ones involving torsion pendulums and floating microdisks^{20–24}, but no measurements have been reported. In the non-retarded regime, in which the effects of quantum fluctuations are considered to be communicated instantly between the bodies, the Casimir torque is equivalent to an anisotropic van der Waals interaction. These short-range interactions can cause alignment of nematic liquid crystals, a phase of matter with ordered molecular orientations often used in display technology. Although many commercial technologies rely on the alignment of liquid crystals on a substrate, the complex alignment mechanisms are not completely understood; however, micrometre-scale surface indentations, stretched polymer chains and optical anisotropy of the substrate are all thought to have important roles. Independent experiments^{25–28} strongly suggest that anisotropic van der Waals torques are sufficient to cause liquid-crystal anchoring. Together, these experiments demonstrated that liquid-crystal anchoring is influenced by the birefringence of a substrate and weakened by a surfactant. However, the angular and distance dependence of this interaction is unknown.

Our experimental design allows us to measure the torque via the twist of a liquid crystal (which acts as a birefringent body) in close proximity to a solid birefringent substrate with a variable spacer layer of thickness d (Fig. 1). This set-up builds on a previously proposed geometry²⁹ and enables precise optical detection of the crystal rotation³⁰. We perform measurements using a common liquid crystal (5CB) and four crystal substrates to ensure robustness of the experiments and to probe different predictions about the sign and magnitude of the Casimir torque. The substrates are calcite (CaCO_3), lithium niobate (LiNbO_3), rutile (TiO_2) and yttrium vanadate (YVO_4) coated with a thin isotropic layer of Al_2O_3 , which acts as a spacer layer (Fig. 1b, Extended Data Fig. 1). Fluorosurfactant FC-4430 (3M) is added to the 5CB at a mass concentration of 0.5% to eliminate liquid-crystal sticking at the interface²⁸. Opposite the crystal substrate is a glass slide coated in polyvinyl alcohol (PVA), which is rubbed to induce anchoring along a fixed angle θ_{rub} (all angles here are relative to the extraordinary axis of the crystal substrate; Fig. 1). The Casimir torque on the 5CB molecules near the solid birefringent substrate causes a twist that propagates through the bulk of the liquid crystal. Using the Oseen–Frank free energy³¹, the torque M per unit area A is $M/A = k_{22}\Delta\theta/t$ on the layer nearest to the crystal substrate³⁰, where $\Delta\theta = \theta_{\text{rub}} - \theta$ is the liquid-crystal twist (typically one to several degrees in our experiments), θ is the angle between the liquid-crystal director and the extraordinary axis of the crystal substrate, k_{22} is the elastic constant of the twist ($3.6 \pm 0.3 \text{ pN}$)³² and t is the measured thickness of the liquid-crystal layer (about $50 \mu\text{m}$). For a torque of the form $M/A = a\sin(2\theta)$, the amplitude of the torque a is calculated as $a = k_{22}\Delta\theta/[t\sin(2\theta)]$.

The Casimir torque that we measure has a $\sin(2\theta)$ dependence for all four birefringent substrates, and the sign and magnitude of the torque depends on the optical properties of the crystals (Fig. 2). To probe the angular dependence, we deposit 6 nm of Al_2O_3 on four different birefringent substrates and assemble cells with circularly rubbed PVA counterplates (Methods). This produces a uniform distribution of θ_{rub} , which allows us to measure the torque as a function of θ using an optical polarimetric measurement set-up (see Methods). All four crystal substrates show a $\sin(2\theta)$ dependence of the torque, with a sign corresponding to the rotation needed to align the principal optical axes with the highest refractive index in the visible portion of the spectrum.

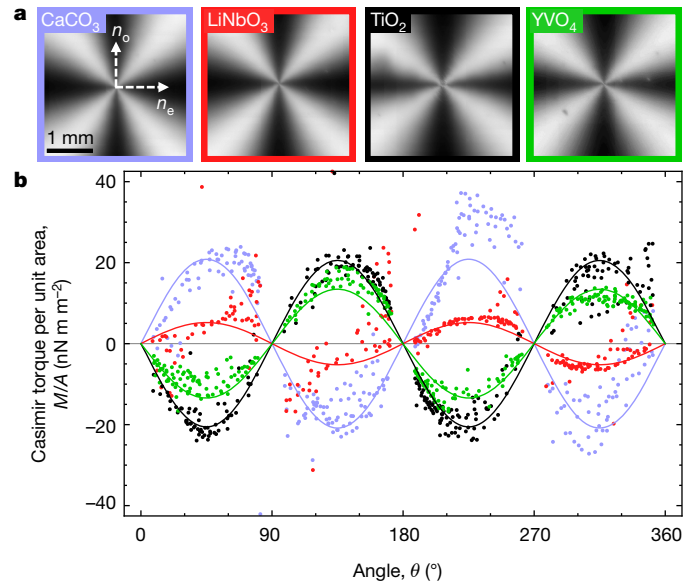


Fig. 2 | Measured $\sin(2\theta)$ angular dependence of the Casimir torque. **a**, Polarized optical micrographs of cells with circularly rubbed PVA and four different birefringent substrates separated by about 18 nm from the birefringent liquid crystal. In each case, the dark brushes along the preferred axis are narrowed: ordinary axis n_o for CaCO_3 and LiNbO_3 , and extraordinary axis n_e for TiO_2 and YVO_4 . **b**, Measured torque (dots) across each cell (colour-coded) as a function of θ . Fits (solid lines) to $\sin(2\theta)$ are overlaid.

The microscope images of the samples between crossed polarizers (Fig. 2a) show the broken symmetry caused by the Casimir torque: in each case, the dark regions are narrowed along the preferred alignment axis. The data are collected at all positions, sorted into 1° bins and fitted with a $\sin(2\theta)$ function to determine the amplitude of the torque (Fig. 2b, solid lines). Control experiments with isotropic glass substrates show no evidence of a torque (Extended Data Fig. 2).

We determine the distance dependence of the Casimir torque using 27 different Al_2O_3 thicknesses (0–25 nm) per crystal substrate and measure the rotation angle to determine the maximum torque at each separation. For these experiments, the PVA layer is rubbed to $\theta_{\text{rub}} \approx 45^\circ$ and nine separations are measured on a single 1-cm² sample (Fig. 1d). Three samples are constructed for each of the four crystal types to achieve 27 distinct separations (Fig. 3). We determine the maximum torque per area for each separation to be $M_{\text{max}}/A = a\sin(90^\circ) = k_{22}\Delta\theta/[t\sin(2\theta)]$. To compare these measurements with the full Casimir-torque calculation, we include a 12-nm offset in the distance between the interacting crystals due to the surfactant, which we assume forms an isotropic layer of constant effective thickness on the substrate, and to sample roughness (see Extended Data Fig. 3 for further details). The torque is calculated using a previously described method³⁰. We find agreement between the measured (Fig. 3, symbols) and calculated (solid lines) values of the torque to within the uncertainties in the measurements and in the tabulated optical properties.

The sign of the Casimir torque depends on the optical properties of the interacting birefringent crystals and can be changed from positive to negative. We categorize these birefringent materials by the sign of the difference in refractive index $\Delta n = n_e - n_o$ and dielectric constant $\Delta\varepsilon_0 = \varepsilon_{0,e} - \varepsilon_{0,o}$ between the ordinary ('o' subscript) and extraordinary ('e' subscript) axes for wavelengths in the visible range and at zero frequency (see Extended Data Fig. 4 for optical properties). TiO_2 and YVO_4 crystals, for which $\Delta n > 0$ and $\Delta\varepsilon_0 > 0$, cause 5CB ($\Delta n > 0$, $\Delta\varepsilon_0 > 0$) to twist towards the extraordinary axis, resulting in a negative torque (Fig. 3). LiNbO_3 has $\Delta n < 0$ and $\Delta\varepsilon_0 < 0$ but weaker anisotropy, which causes a smaller twist towards the ordinary axis and a positive torque. CaCO_3 ($\Delta n < 0$, $\Delta\varepsilon_0 > 0$) is a special case: low-frequency fluctuations should contribute to a torque on 5CB towards

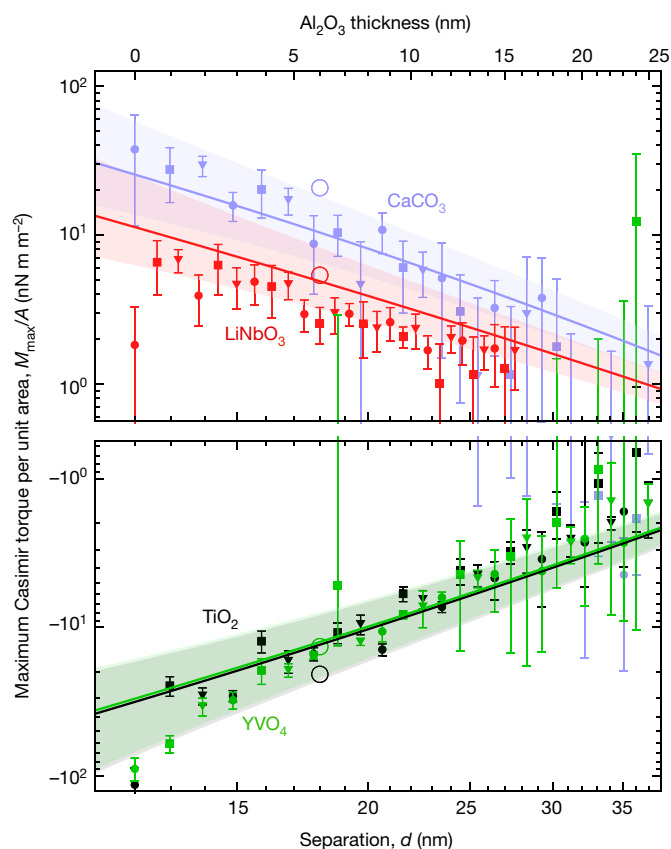


Fig. 3 | Distance dependence of Casimir torque. We measured the amplitude of the Casimir torque between 5CB and four birefringent substrates— CaCO_3 (purple), LiNbO_3 (red), TiO_2 (black) and YVO_4 (green)—as function of separation d . The separation includes the known Al_2O_3 thickness and a constant offset of 12 nm due to the surfactant and the surface roughness. Solid lines represent the calculated torque; shaded regions correspond to the range of values resulting from a range of constant offsets from 8 nm to 16 nm. Error bars denote the standard deviation of the torques measured at different locations within each region and the different types of filled symbol represent different samples of the same crystal type. The open circles represent the amplitudes of the fitted $\sin(2\theta)$ curves from Fig. 2b.

the extraordinary axis, and higher-frequency fluctuations should contribute to a torque of opposite sign towards the ordinary axis. The full Casimir-torque calculation using the available dielectric data predicts that the higher-frequency terms should dominate at the separations in our experiment, leading to a positive torque. This is consistent with our measurement, which demonstrates a torque towards the ordinary axis. At larger separations, the lower-frequency terms dominate and the sign of the torque should be reversed³³; however, no crossover behaviour is observed (or predicted) within one standard deviation of the data in the distance regime probed in our experiments. Our results are all consistent with the expected signs and relative strengths of the calculated torque. For comparison, the fitted torque amplitudes from the circularly rubbed samples (Fig. 2) are also plotted in Fig. 3 (open circles), demonstrating consistency between the different methods.

We have experimentally verified the existence of the Casimir torque between two optically anisotropic materials and have quantified the distance and angular dependence of this phenomenon. With our technique, we are able to measure torques as small as a few nN m^{-2} and have found the results to agree with calculations of the Casimir torque in terms of both sign and magnitude. The measurements presented here will permit further exploration of other theoretical predictions, such as the role of retardation and dielectric spacer layers in enhancing the torque. Finally, we anticipate that this work will open up new avenues

for using the Casimir torque in nano- and micromechanical systems, microfluidics and the self-assembly of nanostructures, in which the role of quantum vacuum fluctuations are often underexplored.

Online content

Any methods, additional references, Nature Research reporting summaries, source data, statements of data availability and associated accession codes are available at <https://doi.org/10.1038/s41586-018-0777-8>

Received: 9 July 2018; Accepted: 25 October 2018;

Published online 19 December 2018.

- Israelachvili, J. N. *Intermolecular and Surface Forces* (Academic Press, Cambridge, 1992).
- Parsegian, V. A. *Van der Waals Forces* (Cambridge Univ. Press, Cambridge, 2005).
- Autumn, K. et al. Adhesive force of a single gecko foot-hair. *Nature* **405**, 681–685 (2000).
- Casimir, H. B. G. On the attraction between two perfectly conducting plates. *Proc. K. Ned. Akad. Wet.* **51**, 793–795 (1948).
- Parsegian, V. A. & Weiss, G. H. Dielectric anisotropy and the van der Waals interaction between bulk media. *J. Adhes.* **3**, 259–267 (1972).
- Barash, Y. S. Moment of van der Waals forces between anisotropic bodies. *Radiophys. Quantum Electron.* **21**, 1138–1143 (1978).
- Lifshitz, E. M. The theory of molecular attractive forces between solids. *J. Exp. Theor. Phys.* **2**, 73–83 (1956).
- Parsegian, V. A. Nonretarded van der Waals Interaction between anisotropic thin rods at all angles. *J. Chem. Phys.* **56**, 4393–4396 (1972).
- Hopkins, J. C., Podgornik, R., Ching, W.-Y., French, R. H. & Parsegian, V. A. Disentangling the effects of shape and dielectric response in van der Waals interactions between anisotropic bodies. *J. Phys. Chem. C* **119**, 19083–19094 (2015).
- Lamoreaux, S. K. Demonstration of the Casimir force in the 0.6 to 6 μm range. *Phys. Rev. Lett.* **78**, 5–8 (1997).
- Munday, J. N., Capasso, F. & Parsegian, V. A. Measured long-range repulsive Casimir–Lifshitz forces. *Nature* **457**, 170–173 (2009).
- Woods, L. M. et al. Materials perspective on Casimir and van der Waals interactions. *Rev. Mod. Phys.* **88**, 045003 (2016).
- Chan, H. B. et al. Measurement of the Casimir force between a gold sphere and a silicon surface with nanoscale trench arrays. *Phys. Rev. Lett.* **101**, 030401 (2008).
- Banishev, A. A., Wagner, J., Emig, T., Zandi, R. & Mohideen, U. Demonstration of angle-dependent Casimir force between corrugations. *Phys. Rev. Lett.* **110**, 250403 (2013).
- Bordag, M., Klimchitskaya, G. L., Mohideen, U. & Mostepanenko, V. M. *Advances in the Casimir Effect* (Oxford Univ. Press, Oxford, 2009).
- Milton, K. A. *The Casimir Effect* (World Scientific, New York, 2001).
- Milonni, P. W. *The Quantum Vacuum: An Introduction to Quantum Electrodynamics* (Academic Press, Cambridge, 1993).
- Decca, R. S., López, D., Fischbach, E. & Krause, D. E. Measurement of the Casimir force between dissimilar metals. *Phys. Rev. Lett.* **91**, 050402 (2003).
- Torricelli, G. et al. Switching Casimir forces with phase-change materials. *Phys. Rev. A* **82**, 010101 (2010).
- Chen, X. & Spence, J. C. H. On the measurement of the Casimir torque. *Phys. Status Solidi B* **248**, 2064–2071 (2011).
- Guérou, R., Genet, C., Lambrecht, A. & Reynaud, S. Casimir torque between nanostructured plates. *Europhys. Lett.* **111**, 44001 (2015).
- Munday, J. N., Iannuzzi, D., Barash, Y. & Capasso, F. Torque on birefringent plates induced by quantum fluctuations. *Phys. Rev. A* **71**, 042102 (2005).
- Munday, J. N., Iannuzzi, D. & Capasso, F. Quantum electrodynamic torques in the presence of Brownian motion. *New J. Phys.* **8**, 244 (2006).
- Rodrigues, R. B., Neto, P. A. M., Lambrecht, A. & Reynaud, S. Vacuum-induced torque between corrugated metallic plates. *Europhys. Lett.* **76**, 822–828 (2006).
- Dubois-Violette, E. & De Gennes, P. G. Effects of long range van der Waals forces on the anchoring of a nematic fluid at an interface. *J. Colloid Interface Sci.* **57**, 403–410 (1976).
- Schadt, M., Schmitt, K., Kozinkov, V. & Chigrinov, V. Surface-induced parallel alignment of liquid crystals by linearly polymerized photopolymers. *Jpn. J. Appl. Phys.* **31**, 2155–2164 (1992).
- Lu, M. Liquid crystal orientation induced by van der Waals interaction. *Jpn. J. Appl. Phys.* **43**, 8156–8160 (2004).
- Bryan-Brown, G. P., Wood, E. L. & Sage, I. C. Weak surface anchoring of liquid crystals. *Nature* **399**, 338–340 (1999).
- Smith, E. R. & Ninham, B. W. Response of nematic liquid crystals to van der Waals forces. *Physica* **66**, 111–130 (1973).
- Somers, D. A. T. & Munday, J. N. Rotation of a liquid crystal by the Casimir torque. *Phys. Rev. A* **91**, 032520 (2015).
- Frank, F. Liquid crystals. On the theory of liquid crystals. *Discuss. Faraday Soc.* **25**, 19–28 (1958).
- Toyooka, T., Chen, G., Takezoe, H. & Fukuda, A. Determination of twist elastic constant K_{22} in 5CB by four independent light-scattering techniques. *Jpn. J. Appl. Phys.* **26**, 1959–1966 (1987).
- Thiyam, P. et al. Distance-dependent sign reversal in the Casimir–Lifshitz torque. *Phys. Rev. Lett.* **120**, 131601 (2018).

Acknowledgements This work was supported by the National Science Foundation under grant numbers PHY-1506047 and PHY-1806768. We acknowledge support from the FabLab at the Maryland NanoCenter and thank M. S. Leite for discussions and comments on the manuscript.

Reviewer information *Nature* thanks O. Lavrentovich, S. Zumer and the other anonymous reviewer(s) for their contribution to the peer review of this work.

Author contributions J.N.M. conceived and supervised the project. D.A.T.S. designed the apparatus, performed experiments and analysed the resultant data. J.L.G. and K.J.P. performed AFM experiments and analysis, and K.J.P. performed spectroscopic ellipsometric measurements and analysis. All authors discussed and interpreted the data and wrote the manuscript.

Competing interests The authors declare no competing interests.

Additional information

Extended data is available for this paper at <https://doi.org/10.1038/s41586-018-0777-8>.

Supplementary information is available for this paper at <https://doi.org/10.1038/s41586-018-0777-8>.

Reprints and permissions information is available at <http://www.nature.com/reprints>.

Correspondence and requests for materials should be addressed to J.N.M.

Publisher's note: Springer Nature remains neutral with regard to jurisdictional claims in published maps and institutional affiliations.

METHODS

Atomic layer deposition. The Al_2O_3 layers are deposited by atomic layer deposition (Beneq) at 150 °C and 3 mbar. The growth rate is measured by deposition on silicon wafers to be 0.12 nm per cycle, and the thickness varies by less than 1 nm over a 1-cm² region. To change the Al_2O_3 thickness on a single sample, different regions are masked using Kapton tape. For each type of crystal, three substrates are coated identically with nine different thicknesses (in intervals of 3j cycles, where $j = 5$ for LiNbO_3 and $j = 8$ for the other crystals) in four deposition steps (Fig. 1d). With two more deposition steps, the three substrates receive an additional deposited layer of 0, j or 2j cycles, resulting in interlaced Al_2O_3 thicknesses across the three substrates. Before each deposition step, the substrates are cleaned with acetone, methanol and isopropanol, dried with N_2 , and placed in a UV/ozone cleaner (Ossila) for 3 min to remove any remaining contaminants.

Construction of the liquid-crystal cell. To make the rubbed PVA slides, borosilicate glass cover slips are cleaned using the same procedure described above. They are spin-coated with 1% PVA in water at 2,000 r.p.m. for 30 s and dried on a hot plate at 105 °C for 30 min. They are then rubbed with a velvet cloth to cause strong liquid-crystal anchoring at the interface (micrometre-scale surface indentations, stretched polymer chains and optical anisotropy of the substrate are all thought to have important roles in the alignment^{34,35}). For circular cells (Figs. 1c and 2), the glass slides are mounted onto a motor that spins them while the cloth is lowered to contact for around 30 revolutions. For linearly rubbed cells (Figs. 1d and 3), the slides are rubbed 30 times unidirectionally. The cells are assembled by cleaning the Al_2O_3 -coated crystals with solvents and UV/ozone as above, placing dots of UV-curable glue (Norland Optics NOA68) mixed with 50- μm spacer beads (Cospheric) in the corners of the sample. They are then pressed to the rubbed PVA slide, cured for 5 min with UV light, placed onto a hotplate at 55 °C, and filled with the liquid-crystal mixture in the isotropic phase (0.5% FC-4430 in 5CB) via capillary action. The hot plate is then turned off and the samples are allowed to cool to room temperature for 1 h before measurement. The FC-4430 covers both surfaces and probably reduces the anchoring strength at the rubbed PVA layer as well as at the crystalline substrate. However, the anchoring at the rubbed PVA remains many orders of magnitude stronger than the Casimir torque, and the liquid-crystal alignment direction remains indistinguishable from the rubbing direction at the top of the cell.

Optical polarimetric measurement. We measure the liquid-crystal anchoring with polarized microscopy (Nikon Eclipse Ti-U; Fig. 1b). First, the sample is rotated so that the extraordinary axis of the solid crystal is aligned with a fixed polarizer. With this orientation, the polarized light passes through the solid crystal without any effect from its birefringence. The illuminated spot is narrowed to a 400- μm diameter with an aperture iris to permit spatial mapping of the liquid-crystal anchoring. An analyser is then rotated in 7.5° increments and the transmitted light passes through a custom-made liquid-crystal depolarizer before being directed into a spectrometer (Thorlabs CCS175). The intensity of the transmitted light as a function of wavelength and analyser angle (θ_a) is recorded (Extended Data Fig. 5b, c) and modelled using Jones calculus (Extended Data Fig. 5d, e):

$$I = \cos^2(X) + \cos^2(\Delta\theta - \theta_a) + \Delta\theta \cos(X) \sin[2(\Delta\theta - \theta_a)] \frac{\sin(X)}{X} + \left[(\Delta\theta)^2 \sin^2(\Delta\theta - \theta_a) + \frac{(\Delta\varphi)^2}{4} \cos^2(\Delta\theta - \theta_a + 2\theta) \right] \frac{\sin^2(X)}{X^2} \quad (1)$$

where $X = \sqrt{\Delta\varphi^2/4 + \Delta\theta^2}$ and $\Delta\varphi = 2\pi\Delta n \times t/\lambda$ is the optical retardance of the liquid-crystal layer with birefringence Δn , thickness t and wavelength λ . A nonlinear fitting algorithm is used to extract $\Delta\theta$ and θ at each point. To obtain a fit, t is first fitted using the known birefringence of 5CB³⁶, and then the birefringence Δn is allowed to vary slightly (at most 0.3%) with fixed t in the nonlinear fit. This step is necessary because small errors in Δn (for example, due to small temperature variations) make a reasonable fit impossible. As a consistency check, fits with Δn values that vary by more than 0.3% at any wavelength from the known curve are rejected.

Data analysis. Using a motorized microscope stage, about 625 local polarized spectrometry measurements were taken across each 1-cm² cell (Extended Data Fig. 5).

We select the data that correspond to a particular region (such as that corresponding to a single Al_2O_3 thickness). Extreme outliers (those that lie more than six times the interquartile range from the median), which can arise from local defects in the cell, are rejected. The remaining data are summarized with a mean and standard deviation.

Measurement sensitivity. In order of decreasing importance, the sensitivity of our measurement is limited by non-uniformities in the liquid-crystal cells, the optical measurement technique and Brownian motion. The first of these is the dominating factor in our measurements and can be estimated by the large-separation torques in Fig. 3. At large separations for LiNbO_3 , TiO_2 and YVO_4 , we can resolve torques with magnitudes of about $3 \times 10^{-9} \text{ N m m}^{-2}$ (several orders of magnitude smaller than typical ultraweak liquid-crystal anchoring energies; the FC-4430 is used to greatly reduce these energies so that the Casimir-torque energy is the dominant interaction). The CaCO_3 substrates are more susceptible to surface defects in fabrication, which limits the sample quality.

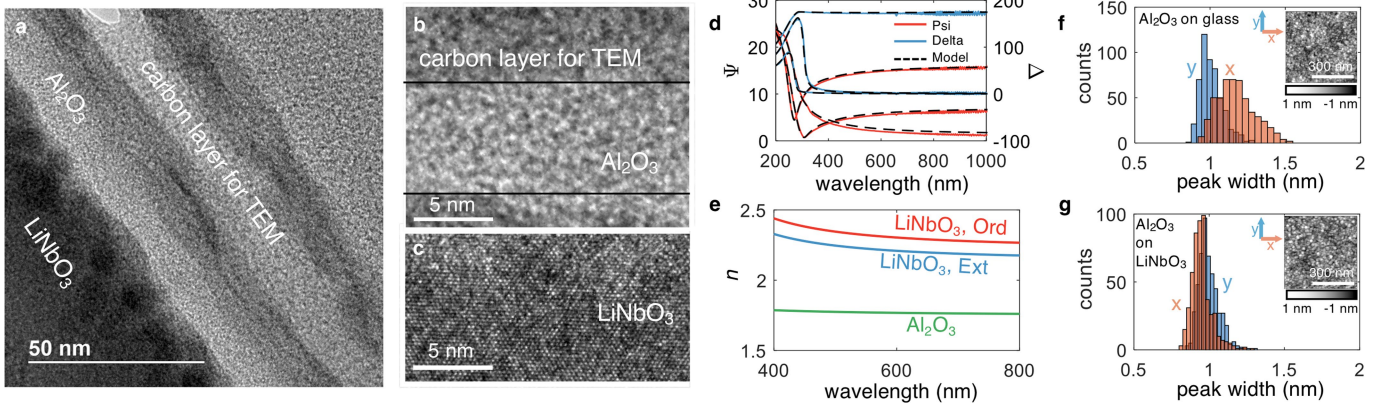
With an ideal fabrication process that produces uniform and defect-free samples, the optical measurement would limit the sensitivity. From the torque balance equation $a \sin(2\theta) = k_{22}\Delta\theta/t$, the smallest measurable torque is limited by the smallest measurable twist angle $\Delta\theta$. For a cell with $t = 50 \mu\text{m}$, a measurement of $\Delta\theta$ with a resolution of 0.1° corresponds to a torque sensitivity of around $10^{-10} \text{ N m m}^{-2}$. The resolution of the torque measurement can be improved by increasing t , but doing so introduces other practical experimental issues, such as polarization-dependent absorption and long-range liquid-crystal defects. For very small values of t (less than 1 μm), the torque resolution would become worse and other fluctuation-induced effects, such as the critical Casimir effect, would need to be considered if the temperature of the cell approaches the liquid-crystal phase transition³⁷.

If all other factors were mitigated, the minimum noise level of our measurement technique would be dominated by thermal noise of magnitude $k_B T$. The measured torque per unit area is $k_{22}\Delta\theta/t$ and the free energy associated with the dependent variable $\Delta\theta$ is $k_{22}(\Delta\theta)^2/(2t)$. Setting this equal to $k_B T/A$ (where A is the area of the measured spot size), we find that the minimum resolvable $\Delta\theta$ due to thermal noise is $\sqrt{k_B T t / (A k_{22})}$. With $T = 300 \text{ K}$, $t = 50 \mu\text{m}$ and $A = 1 \text{ mm}^2$, this is about 0.01°, which corresponds to a best possible torque-per-unit-area sensitivity of about $10^{-11} \text{ N m m}^{-2}$.

Data availability

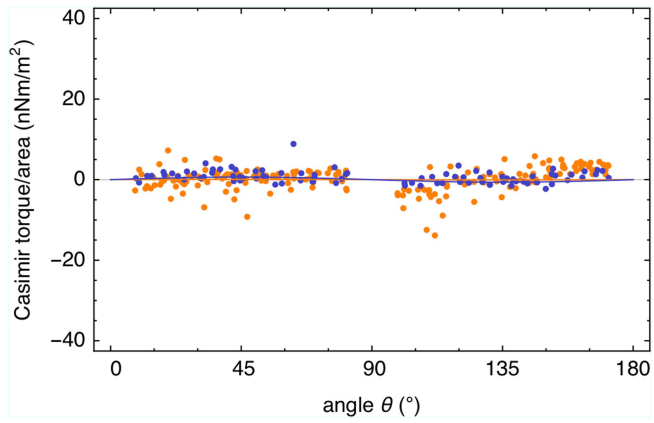
The data that support the findings of this study are available from the corresponding author on reasonable request.

- Ishihara, S. How far has the molecular alignment of liquid crystals been elucidated? *J. Disp. Technol.* **1**, 30–40 (2005).
- Kobayashi, S., Kuroda, K., Matsuo, M. & Nishikawa, M. in *The Liquid Crystal Display Story* (ed. Koide, N.) 59–80 (Springer, Tokyo, 2014).
- Li, J. & Wu, S. T. Extended Cauchy equations for the refractive indices of liquid crystals. *J. Appl. Phys.* **95**, 896–901 (2004).
- Li, H. & Kardar, M. Fluctuation-induced forces between rough surfaces. *Phys. Rev. Lett.* **67**, 3275–3278 (1991).
- Miikkulainen, V., Leskelä, M., Ritala, M. & Puurunen, R. L. Crystallinity of inorganic films grown by atomic layer deposition: overview and general trends. *J. Appl. Phys.* **113**, 021301 (2013).
- Hu, J., Xiao, X. D., Ogletree, D. F. & Salmeron, M. Imaging the condensation and evaporation of molecularly thin films of water with nanometer resolution. *Science* **268**, 267–269 (1995).
- Neuman, K. C. & Nagy, A. Single-molecule force spectroscopy: optical tweezers, magnetic tweezers and atomic force microscopy. *Nat. Methods* **5**, 491–505 (2008).
- Kornilovitch, P. E. Van der Waals interaction in uniaxial anisotropic media. *J. Phys. Condens. Matter* **25**, 035102 (2013); corrigendum **30**, 189501 (2018).
- Hough, D. B. & White, L. R. The calculation of hamaker constants from liftshitz theory with applications to wetting phenomena. *Adv. Colloid Interface Sci.* **14**, 3–41 (1980).
- Shi, H.-s., Zhang, G. & Shen, H.-y. Measurement of principal refractive indices and the thermal refractive index coefficients of yttrium vanadate. *J. Synth. Cryst.* **30**, 85–88 (2001).
- Vali, R. Ab initio vibrational and dielectric properties of. *Solid State Commun.* **149**, 1637–1640 (2009).

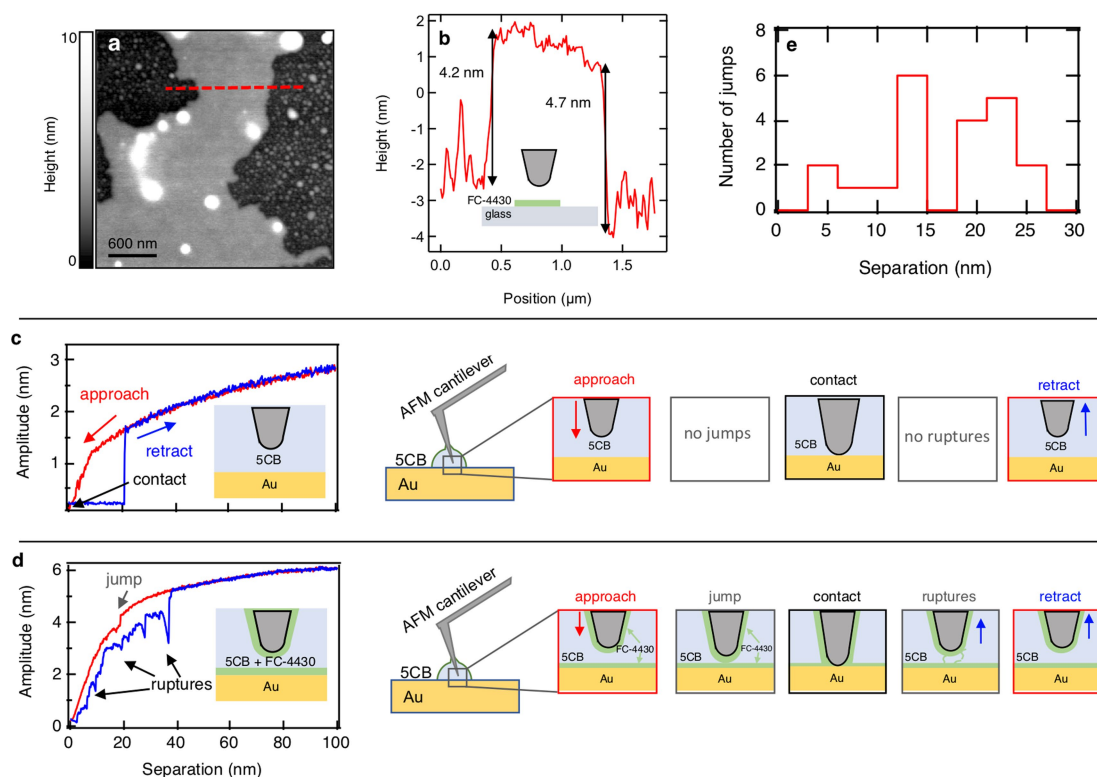


Extended Data Fig. 1 | Evidence for amorphous, isotropic deposition of Al_2O_3 . Atomic layer deposition of Al_2O_3 on planar substrates at low temperatures (in our case 150°C) generally results in isotropic, amorphous films³⁸. To confirm this expectation, we performed three different experiments to characterize the films. **a–c**, First, TEM measurements at different magnifications show that the Al_2O_3 layer is amorphous (**a**, **b**), whereas the LiNbO_3 layer is crystalline (**a**, **c**), as expected. **d**, Second, spectroscopic ellipsometry data are found to be consistent with an isotropic layer of Al_2O_3 existing on top of the birefringent LiNbO_3 crystal. We first determined the optical properties for the birefringent LiNbO_3 crystal without any Al_2O_3 coating. Ψ and Δ data (ellipsometric amplitude and phase ratio, respectively) for 55° , 60° and 75° measurement angles are performed and fitted to a Tauc Lorentz biaxial (anisotropic) model, yielding a good ellipsometric fit. **e**, Third, spectroscopic ellipsometry was performed on a LiNbO_3 crystal with a 5-nm-thick Al_2O_3 coating. The previously determined model for LiNbO_3 was used together with an isotropic model for Al_2O_3 , yielding a similarly good fit with no increase in the mean squared error. A birefringent model for Al_2O_3 could also be

used; however, this results in additional fit parameters that artificially reduce the mean squared error below that obtained with the LiNbO_3 crystal alone, providing strong evidence that the isotropic model of Al_2O_3 is more physical. The resulting indices of refraction n are shown for both the ordinary ('Ord') and extraordinary ('Ext') axes of LiNbO_3 and for isotropic Al_2O_3 . **f**, **g**, Fourth, to rule out potential in-plane anisotropy due to correlation in the orientation of the surface roughness, we performed atomic force microscopy (AFM) topography scans of the Al_2O_3 surface as-deposited for our glass control samples (**f**) and the LiNbO_3 crystal (**g**). The roughness is randomly oriented with no preferred direction in both cases. We further considered the widths of the roughness peaks in the two perpendicular directions (x and y in the insets, which show the topography scans). For the Al_2O_3 film on the glass substrate, the average peak widths in the x and y directions are 1.2 ± 0.3 nm and 1.0 ± 0.2 nm, respectively. Similarly, for the Al_2O_3 film on the LiNbO_3 substrate, the average peak widths in the x and y directions are both 1.0 ± 0.2 nm. Although small variations between the x and y scans may be expected due to sample drift or tip geometry, no substantial difference is measured.

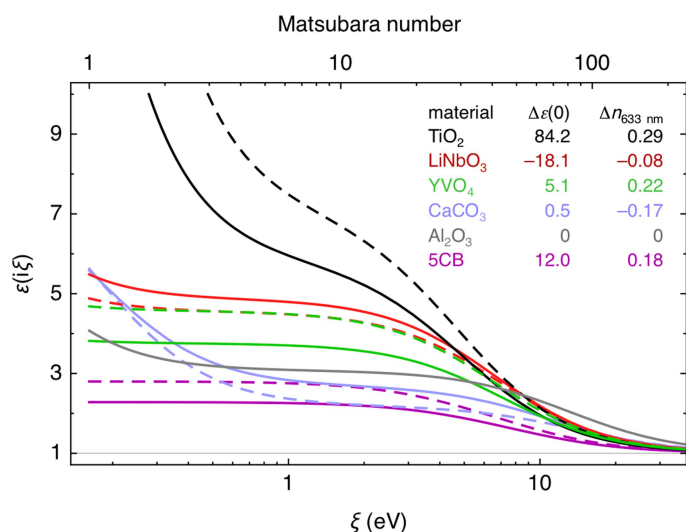


Extended Data Fig. 2 | Control experiment showing no measured torques from isotropic borosilicate glass. Glass substrates are coated with 6 nm of Al_2O_3 (orange) or around 6 nm of PVA (purple). When fitted with a $\sin(2\theta)$ function (solid lines), there is no measurable torque.



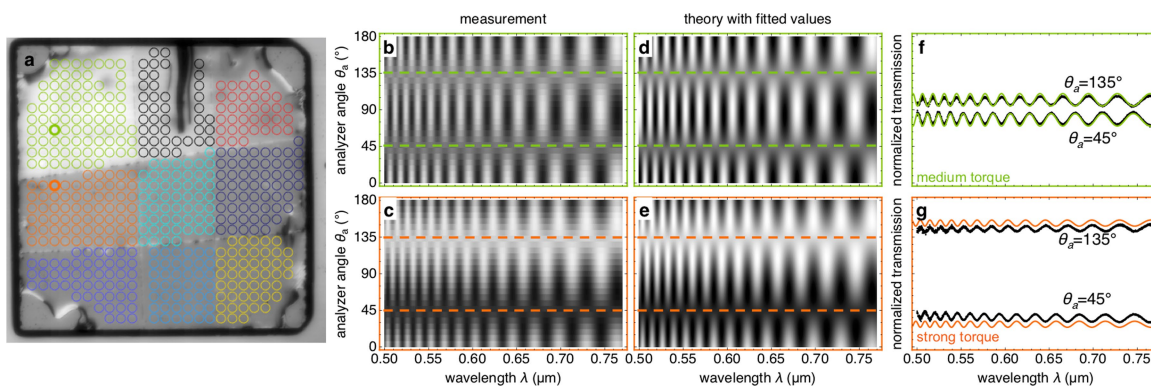
Extended Data Fig. 3 | Determination of the distance offset. We use AFM to probe the thickness of the FC-4430 surfactant layer that forms between the 5CB liquid crystal and the solid substrate, using two different methods^{39,40}. **a**, The first sample was prepared by spreading a 0.5% FC-4430 in 5CB mixture (similar to those used in the torque experiments) across a glass substrate to allow for segregation of the materials. AFM scans (dynamic mode in air to ensure that the optical lever detection scheme of AFM was not distorted by the birefringence of the liquid crystal) show the surfactant monolayer (grey) on glass (black) with 5CB droplets (white). **b**, A line scan across surfactant layer (dashed red line in **a**) shows the step height of the surfactant film on glass to be 4.5 ± 0.3 nm. This measurement puts a minimum bound on the thickness of the surfactant layer, because when immersed in 5CB (as done in the torque experiments) the surfactant molecules will probably extend further from the surface. **c, d**, To determine the total extent of the surfactant in situ, we performed a second set of experiments, using a technique similar to that used in ref. ⁴⁰. For these experiments, a gold sample is used to allow a bias voltage to be applied between the tip and the sample to more accurately determine the exact location of tip-sample contact. **c**, A droplet of 5CB is

placed on the gold sample and a platinum AFM tip is brought towards the surface under 3-V a.c. bias, without any surfactant present. The amplitude of the piezoelectrically driven oscillation of the tip smoothly decreases as it approaches the 5CB-gold boundary, except where the tip sticks to the surface after contact (tip-sample separation of zero). **d**, A second gold sample is used with a droplet of the 0.5% FC-4430 in 5CB mixture (similar to that used in the torque experiments), so that the surfactant covers both surfaces. Again, the amplitude of tip oscillation is recorded during the approach and retract runs under 3-V a.c. bias. On approach, the amplitude decreases rapidly at a certain separation (about 20 nm for this scan), indicating the distance at which the surfactant layers on each surface join together (that is, 'jump' to contact). On retraction, multiple features are observed at locations where molecules attached to both surfaces separate (that is, 'rupture'). **e**, Histogram showing separations at which jumps occur over several distinct distance sweeps. A jump is observed in 21 of 31 approach-retract curves and occurs at an average tip-sample separation of 16.6 nm, which would imply a 8.3-nm-thick surfactant layer on each surface when immersed in 5CB. Considering the measured surface roughness of 4–5 nm, we use a distance offset of 12 ± 4 nm.



Extended Data Fig. 4 | Dielectric models for the relevant materials.

For birefringent materials, solid and dashed lines indicate the dielectric function ε along the ordinary and extraordinary axes, respectively. The dielectric models for the 5CB liquid crystal are from ref. ⁴¹, the dielectric functions for the solid crystals are modelled using a previous method⁴² and the dielectric data for YVO₄ are from refs ^{43,44}. The dielectric function of the thin FC-4430 layer is unknown, but its precise value has little effect on the torque. For our calculations, the layers between the two crystals are treated as a uniform, homogeneous medium described by the optical properties of Al₂O₃ alone (rather than part Al₂O₃ and part FC-4430). As an extreme case, we also calculate the torque with a uniform medium with the optical properties of H₂O, which are probably similar to the unknown FC-4430, rather than Al₂O₃. The calculated torque changes by less than 6% for the distances used in our experiment and are thus within our calculation uncertainties.



Extended Data Fig. 5 | Polarized spectrometry measurement of each sample. a, Polarized white-light image of a 1-cm² substrate (TiO₂) with nine different Al₂O₃ thicknesses achieved through atomic layer deposition and masking. The coloured circles indicate separate polarized spectrometry measurements, two of which (bolded) are shown in more detail in **b–g**. **b, c,** Normalized, measured transmission as a function of analyser angle and wavelength for regions with thick (**b**) and thin (**c**) Al₂O₃ layers. The thick (thin) layer corresponds to a larger (smaller) separation d between the birefringent materials. The dashed lines indicate θ_{rub} and

$\theta_{\text{rub}} - 90^\circ$. **d, e,** Results from fitting **b** and **c** using equation (1) in Methods. **f, g,** Transmitted intensities (dots, measured values; solid lines, theoretical fits) along $\theta_a = \theta_{\text{rub}} = 135^\circ$ and $\theta_a = \theta_{\text{rub}} - 90^\circ = 45^\circ$ are shown for the thick (**f**) and thin (**g**) Al₂O₃ layers. A strong torque causes a larger difference in transmission between $\theta_a = \theta_{\text{rub}}$ and $\theta_a = \theta_{\text{rub}} - 90^\circ$ (compare **g** and **f**). The slight offset between the fit and measurement in **g** is because only two of the 25 measurements used in the fit are plotted. Combining all measurements, the error in the angle is less than 4° .